Topological features dictate the mechanics of the mammalian brains

P. Sáez[a,b,*], C. Duñó[a], L.Y. Sun[c], N. Antonovaite[d], M. Malvè[e,f], D. Tost[c,g], A. Goriely[h]

[a] *Laboratori de Calcul Numeric (LaCaN), Universitat Politècnica de Catalunya, Barcelona, Spain.*
[b] *Barcelona Graduate School of Mathematics–BGSMath, Barcelona, Spain*
[c] *Centre de Recerca en Enginyeria Biomèdica (CREB),Universitat Politècnica de Catalunya, Barcelona, Spain*
[d] *Department of Physics and Astronomy and LaserLab Amsterdam, Vrije Universiteit Amsterdam, De Boelelaan 1085, 1081 HV Amsterdam, Netherlands*
[e] *Centro de Investigación Biomédica en Red en Bioingeniería Biomateriales y Nanomedicina (CIBER-BBN), Aragón Institute of Engineering Research (I3A), Universidad de Zaragoza*
[f] *Department of Engineering, Public University of Navarra, Pamplona, Spain*
[g] *Institut de Recerca Sant Joan de Déu, Barcelona, Spain.*
[h] *Mathematical Institute, University of Oxford, Oxford, UK.*

Abstract

Understanding brain mechanics is crucial in the study of pathologies involving brain deformations such as tumor, strokes, or in traumatic brain injury. Apart from the intrinsic mechanical properties of the brain tissue, the topology and geometry of the mammalian brains are particularly important for its mechanical response. We use computational methods in combination with geometric models to understand the role of these features. We find that the geometric quantifiers such as the gyrification index play a fundamental role in the overall mechanical response of the brain. We further demonstrate that topological diversity in brain models is more important than differences in mechanical properties: Topological differences modify not only the stresses and strains in the brain but also its spatial distribution. Therefore, computational brain models should always include detailed geometric information to generate accurate mechanical predictions. These results suggest that mammalian brain gyrification acts as a damping system to reduce mechanical damage in large-mass brain mammals. Our results are relevant in several areas of science and engineering related to brain mechanics, including the study of tumor growth, the understanding of brain folding, and the analysis of traumatic brain injuries.

Keywords: Brain shape, animal-scale laws, Brain Mechanics, Finite Element Method.

1. Introduction

The mammalian brain is, arguably, the most intriguing and unexplored organ. It acts as a command center for the nervous system where distinct regions are mostly responsible for controlling specific cognitive functions such as perception, emotion, behavior, or motor function. The majority of brain research is focused on understanding the ways in which the brain cognition works. However, brain mechanics, the way in which the brain deforms under external or internal mechanical loads, is fundamental for the analysis of a large number of brain pathologies that are strain-dependent and that modify brain function [11, 67, 25, 24]. For example, tumor growth has been demonstrated to be highly dependent on the mechanical environment [29, 8]. Computational models have been used to quantify the deformation that a brain experiences during tumor progression [57, 62, 2]. Swelling process in the brain induce large deformation in the brain tissue [21, 68, 43] and different mathematical and computational models have been developed to analyze the mechanical response of the brain under such internal loads [26, 15, 44]. Computational models have also been used

*Corresponding author: P. Sáez
Email address: pablo.saez@upc.edu (P. Sáez)

to evaluate mechanical deformations during decompressive craniotomies [16, 19, 70]. Traumatic brain injuries (TBI) depend on the mechanical injury that the brain suffers [22, 54, 72] and many experimental [10, 45, 39, 58] and computational models [38, 17, 41, 71, 42] have been used to evaluate the impact of mechanical loads in brain damage mechanics.

At the tissue level, experimental tests have been conducted to determine the mechanical properties of the brain [51, 18, 12, 6] where a wide range of stiffness values of mammalian brains have been reported. Today, it is accepted that the stiffness of brain tissue is in the range 0.1-4 kPa [37, 6], depending on the brain region probed [40, 3]. Measured through Magnetic Resonance Elastography (MRE), the stiffness of the brain tissue has been measured to be within a range of 1 to 20 kPa [50, 35, 69, 33], but most studies place brain tissues within the 3-6kPa range, close to the values reported by mechanical testing. By means of MRE it was also suggested that there are not variations in tissue stiffness between species [69] and that stiffness differences mainly arise due to tissue composition [40, 3]. The brain tissue also exhibits viscoelastic behavior [53, 12, 6], both at small and large strain although it is still unclear which components of the brain tissue determine the viscoelastic response at the tissue scale. Along with experimental characterizations and modeling efforts, different computational models have been proposed to study the mechanical response of the mammalian brain under static and dynamics loads [49, 63, 34]. At the organ level, computational models are used to predict mechanical states under internal or external mechanical loads, bypassing costly and potentially unethical experimental tests. However, many computational models are not fully reliable because the complexity of the brain geometry under study is not well represented, which is central to many disciplines that involve brain mechanics. In particular, the influence of brain geometry has not been analyzed in computational models and the vast majority of models rely on coarse geometrical representations [55, 36, 52, 66]. Indeed, only a few models have been able to present accurate geometrical reconstruction and perform computational mechanics simulations [41, 64]. Moreover, many experimental and computational models use results from one specific mammalian species to extrapolate mechanical information to another mammalian brain, usually humans. It is therefore key to understand whether the mechanical response of the brains in different animal species under a given mechanical load is equivalent and what are the key brain features that make brain mechanics different from one species to another.

A standard quantifier for brain morphology is the gyrification index (GI) defined as the ratio of total cortical surface to the area of an outer surface (the convex hull) that smoothly encloses the cortex. The GI varies dramatically between species [46] with values close to one for mammals with smooth brains such as manatees and rodents, and as high as 2.5 for the human brain and 2.7 for some odontocetes [59, 48]. Several physical models have demonstrated that mechanics forces control folding during development [25, 61, 32]. However, only few studies have accounted for the effect of small topological features, e.g. sulci, in the mechanics of the brain [14, 30]. Here, we argue that brains with very different folding patterns present very different overall mechanical responses. Specifically, we address two important questions in brain mechanics: What is the role of mammalian brain folding in the mechanics of the brain? How important are topological variations in comparison to the elastic and viscoelastic responses for brain mechanics?

2. Material and Methods

2.1. Image-based geometrical reconstruction

We reconstructed the external surface of three mammalian brains: a human, a macaque and a mouse brain, which represent a GI ≈2.5, 1.75 and 1, respectively. DICOM data (Digital Imaging and Communications in Medicine) were collected from the Center For in Vivo Microscopy at the Duke University Medical Center for the mouse and the manatee models. The mouse brain was

obtained using a wild-type adult male C57BL/6 mouse. The human brain were obtained by means of MRI data collected from the Human Connectome Project (Subject Id: Id 100307). The medical images were manually segmented using the software package 3DSlicer (BSD-style open source, The Open Source Initiative). Each STL file coming from the geometrical segmentation was imported in the commercial software Rhinoceros for a further smoothing and merging of the different parts composing every single brain model to obtain surfaces that compose the 3D geometry, an STL (Stereo Lithography) file.

2.2. Generation of the computational grid

The reconstructed STL files containing the various parts of each brain model (cerebellum, left and right cerebrum, gray matter, cranium etc....) were imported into the commercial computer aided design software (CAD) Rhinoceros (McNeel and Associates, Indianapolis, IN, USA). With this software, all the brain structures were merged in one single model for each considered case. Each complete model was finally exported and used to create 3D computational grids. Fig. 1 shows the resulting geometry models of the three mammal brains. The meshes were generated by means of the commercial software package Ansys IcemCFD (Ansys Inc., Canonsburg, Pennsylvania, USA). The STL files containing the compete model of the rat, the macaque and the human brain were separately imported into Ansys IcemCFD. Due to the intrinsic complexity of the brain geometry that is composed by several tortuous regions, an unstructured topology was selected. The semi-automated octree algorithm of Ansys IcemCFD was used to generate the unstructured tetrahedral grids by assigning separate surface cell sizes to different geometric parts and an overall grid expansion ratio. The first preliminary step for grid generation was to split-up the geometry into multiple surface parts, which permitted regional specification of grid resolution. With this aim, a multiple external and internal surfaces were defined, permitting variable cerebrum and cerebrospinal fluid grid refinement. The element size, that is the minimum length of any side of all tetrahedral elements in the model, should be enough small to acceptably discretize the model volume. In the other side, it is well known that an excessive number of elements may results in an increase of computational costs. For this reason, for establishing the adequate element size for each model, a mesh independence analysis was carried out. Different resolutions were considered progressively increasing the element size and a structural analysis was performed in each case. The computed strains were compared among different mesh resolutions. After this analysis, the element size selected for the mouse resulted in 0.1 mm, for the macaque was 0.7 mm and for the human brain resulted in 1.2 mm. This means that meshes using smaller element sizes resulted in an increase of computational time without adding precision to the numerical solution while coarser grids resulted inadequate. The mouse brain was composed of 67820 nodes and 33914 elements. The brain tissue was composed of 27298 elements and 54592 nodes and the CSF section was made of 6616 elements and 13228 nodes. The macaque model was composed by 295302 elements and 590640 nodes. The brain tissue was composed by 528472 nodes and 264216 elements and the CSF was made of 31086 nodes and 62168 elements. Finally, the human model was composed of 2,062,416 elements for the CSF. The grey and white matter are made of 1,678,496 and 5,301,024 elements, respectively. The right and left hemisphere of the gray matter have 844,640 and 833,856 elements respectively. The white matter is made of 777,952 and 782,160 for the right and left side respectively. Multiple smoothing iterations were carried out for improving the grid quality.

2.3. Mechanical testing of the brain tissue

We provide here a basic explanation of how the mechanical tests were performed (see [3] for more details). Horizontal brain tissue slices of 300 um thickness were extracted from 6 months old C57 / BL6(Harlan) mouse. All experiments were performed in accordance with protocols and

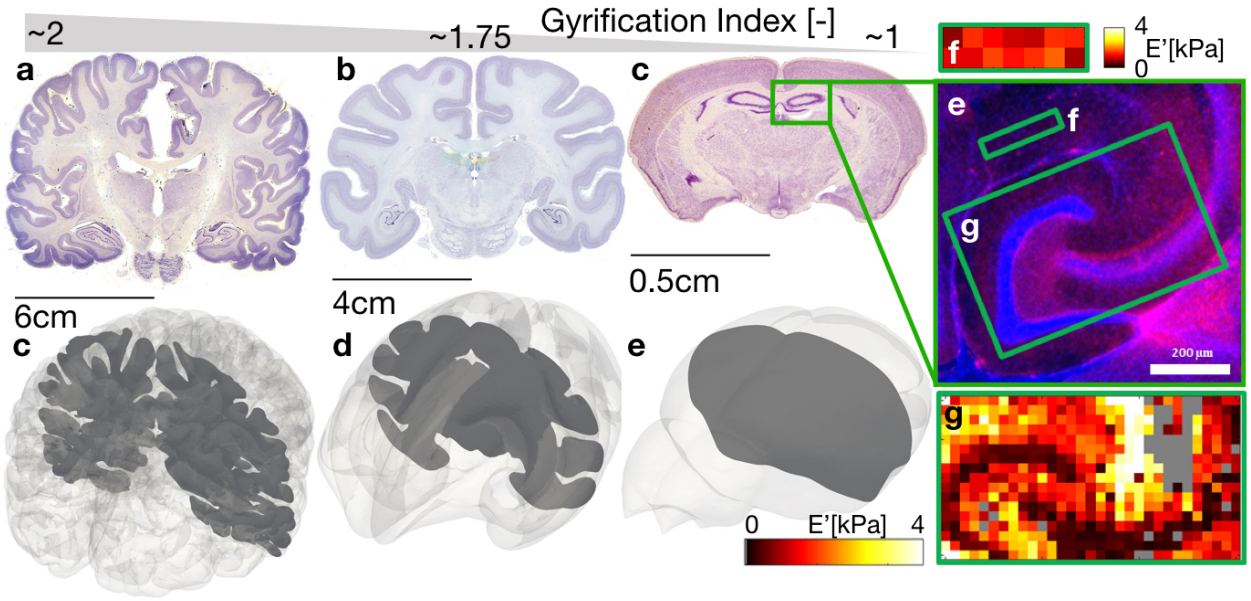

Figure 1: Coronal sections of a human (a), rhesus macaque (b) and common mouse (c) brain (adapted from http://brainmuseum.org). Reconstruction of a finite element mesh for the three species (d-f). Fluorescence image of hippocampus stained for nuclei (Hoechst). Storage modulus map over regions with low density of axons and cells obtained at 6.6% strain, 5.62Hz frequency with equilibrium frequency sweep (f). Storage modulus map of other hippocampal regions at 6.6% strain, 5.62Hz frequency previously obtained with oscillatory ramp (g)[3].

guidelines approved by the Institutional Animal Care and Use Committee (UvA-DEC) operating under standards set by EU Directive 2010/63/EU. Sample was placed in a glass bottom chamber for imaging with inverted microscope, supplied with carbonated artificial cerebrospinal fluid to maintain the viability and gently pressed down with harp for stabilization. Measurements were performed within 6 hours after extraction.

Indentation setup consist of a cantilever-based Ferrule-top probe (k=0.2 N/m, R=95 um) equipped with interferometric readout mounted on a piezo transducer and XYZ manipulator (more details [3]). Indentation was performed in an indentation-depth controlled mode at 5 um/s indentation speed, up to 10 um depth, followed by 30 s load relaxation and frequency sweep between 1Hz and 10 Hz. Stratum lacunosum-moleculare region situated in hippocampus was selected for the measurements due to relatively low density of cells and axons. In comparison to white matter we can see that density of axons is low here. The fluorescence image of the region of interest and the storage modulus map obtained from a Hertz model is shown in Fig. 1.

2.4. Kinematics of the brain dynamics problem

We use the theory of nonlinear elasticity [27]. We characterize the spatial motion problem is through the spatial motion map,

$$\mathbf{x} = \boldsymbol{\chi}\,(\,\mathbf{X}, t\,)\;:\qquad \Omega_0 \to \Omega_t, \tag{1}$$

between the material placement $\mathbf{X}$ of a particle in Ω_0, to the spatial placement $\mathbf{x}$ of the same particle in the spatial configuration Ω_t. The deformation gradient $\mathbf{F}$ and its Jacobian J are defined then as

$$\mathbf{F} = \nabla_X \boldsymbol{\chi}\,(\mathbf{X}, t)\;:\qquad T\Omega_0 \to T\Omega_t \qquad J = \det \mathbf{F} > 0, \tag{2}$$

representing the linear tangent map from the tangent space $T\Omega_0$ to the time–dependent tangent space $T\Omega_t$. We also define the right spatial Cauchy– Green strain tensor $\mathbf{C} = \mathbf{F}^t \cdot \mathbf{F}$. Finally, we define the material time derivative D_t of the spatial velocity $\mathbf{v} = \mathrm{D}_t \boldsymbol{\chi}(\mathbf{X}, t)$.

2.5. Balance of linear momentum

The mass specific version of the balance of linear momentum is based on the kinetic energy density, $K = \frac{1}{2}\mathbf{v} \cdot \mathbf{v}$. The motion momentum density $\mathbf{p}$ is defined by the partial derivative with respect to the spatial velocity $\mathbf{v}$ as

$$\mathbf{p} = \partial_{\mathbf{v}} K = \mathbf{v} \tag{3}$$

The rate of change of the mass specific spatial motion momentum density $\mathbf{p}$ is balanced with the momentum fluxes $\boldsymbol{\sigma}$ and the reduced momentum sources $\mathbf{b}$ as

$$\rho \mathrm{d}_t \mathbf{p} = \nabla \cdot \boldsymbol{\sigma} + \mathbf{b} \tag{4}$$

where the Neumann boundary are

$$\boldsymbol{\sigma} \cdot \mathbf{n} = \mathbf{t} \tag{5}$$

2.6. Constitutive equations in brain dynamics

We model the tissue as a quasi-incompressible hyperelastic material with a viscoelastic component and use the framework of large strains theory, that relies on the definition of a strain-energy density function (energy for short) $\Psi(\bar{\mathbf{C}})$. The quasi-incompressible behavior of the tissue is reproduced through a volumetric-isochoric decomposition of the deformation gradient, which was first proposed by [20]. The deformation gradient $\mathbf{F}$ is decoupled into dilatational and volume-preserving part as $\mathbf{F} = \mathrm{J}^{1/3}\bar{\mathbf{F}}$, where $\bar{\mathbf{F}}$ is the isochoric deformation gradient. Consequently, we split the energy as

$$\Psi(J, \bar{\mathbf{C}}) = \Psi_{\mathrm{vol}}(J) + \Psi_{\mathrm{ich}}(\bar{\mathbf{C}}), \tag{6}$$

where Ψ_{vol} is related with the water content in the brain. The second term $\Psi_{\mathrm{ich}}(\bar{\mathbf{C}})$ is associated with the isochoric contribution of the deformation gradient, which is associated with the solid components of the tissue and $\bar{\mathbf{C}}$ corresponds with the right Cauchy Green tensor. The isochoric contribution can again be split up into different parts to model the behavior of the different components. In terms of the mechanical behavior of the brain tissue, we consider the gray matter to be mechanically isotropic. On the other hand, white matter can be described as anisotropic due to axonal structure lining in a preferential direction as it has been described in [41]. In this contribution and for sake of analyzing exclusively the mechanics of the folding pattern, we consider also the white matter as isotropic. The elastic response of the both the gray and white matter is fully characterized by a Mooney-Rivlin energy function

$$\Psi_{\mathrm{iso}}(\overline{I}_1, \overline{I}_2) = C_{10}[\overline{I}_1 - 3] + C_{01}[\overline{I}_2 - 3] \tag{7}$$

where C_{10} kPa and C_{01} kPa are material parameters and $\overline{I}_1 = tr(\bar{\mathbf{C}})$ and $\overline{I}_2 = 0.5\,\overline{I}_1^2 - (\bar{\mathbf{C}} \cdot \bar{\mathbf{C}})]$ are the first and second invariant of the isochoric part of the deformation. The elastic Piola-Kirchhoff stress tensor is then given by

$$\mathbf{S} = 2\partial_{\mathbf{C}}\Psi_{\mathrm{vol}} + 2\partial_{\mathbf{C}}\Psi_{\mathrm{ich}}(\bar{\mathbf{C}}) = \mathbf{S}_{\mathrm{vol}} + \mathbf{S}_{\mathrm{ich}}, \text{ with} \tag{8}$$

$$\mathbf{S}_{\mathrm{vol}} = 2\partial_{\mathbf{C}}\Psi_{\mathrm{vol}} \qquad \text{and} \qquad \mathbf{S}_{\mathrm{ich}} = 2\partial_{\bar{\mathbf{C}}}\Psi_{\mathrm{ich}}(\bar{\mathbf{C}}) : \partial_{\mathbf{C}}\bar{\mathbf{C}} = \mathrm{J}^{-2/3}\mathbb{P} : \bar{\mathbf{S}} \tag{9}$$

the volumetric and isochoric Piola-Kirchhoff stress tensor. $\bar{\mathbf{S}} = \partial_{\bar{\mathbf{C}}}\Psi_{\mathrm{ich}}(\bar{\mathbf{C}})$ is the fictitious second Piola-Kirchhoff stress and $\mathbb{P}$ is the fourth order projection tensor in the material reference defined as $\mathbb{P} = \mathbb{I} - 1/3\mathbf{C}^{-1} \otimes \mathbf{C}$. Then, we recover the Cauchy stress tensor as $\boldsymbol{\sigma} = \mathbf{F} \cdot \mathbf{S} \cdot \mathbf{F}^T$

Average 14 samples	C_{10} [Pa]	C_{01} [Pa]	g_1 [-]	τ_1 [s]
Mean	668	431	0,90	10,5
Standard deviation	175	207	0,02	3,5

Table 1: Averaged values of the elastic and viscoelastic parameters. The equivalent shear modulus of the tissue based on the values of the Mooney-Rivlin model (C_{10}=668Pa C_{01}=441Pa) is $\mu = 2(C01 + C01)$ ≈2.2kPa and the Young's modulus is E=6.6kPa. These two values of shear and Young modulus are within the range of values reported in literature (see the Introduction section).

To include the viscoelastic behavior, we use a one-term Prony formulation which is a powerful method for modeling of soft tissues [6]. The evolution of stiffness moduli in time is then given by

$$\mathrm{C}_i(t) = \mathrm{C}_{i_0}\left[1 - g_1[1 - e^{-(t/\tau_1)}]\right], \tag{10}$$

where g_1 is the characteristic time constants of the material and τ_1 is the the stiffness weight associated with the time constant. At long enough tomes, we obtain the steady-state moduli $\mathrm{C}_{i_\infty} = \mathrm{C}_{i_0}[1 - g_1]$.

We use the convolution integral to include the Prony series in the Mooney-Rivlin material model as

$$\Psi_{\mathrm{iso}}(\overline{I}_1, \overline{I}_2) = \int_0^t \left[C_{10}(t-\tau)\frac{[\overline{I}_1 - 3]}{\partial\tau} + C_{01}(t-\tau)\frac{[\overline{I}_2 - 3]}{\partial\tau}\right] d\tau \tag{11}$$

Note that we work with the deviatoric part of the energy as the volumetric behavior is assumed to be time independent. τ are the time decay constant.

We make use of a genetic algorithm strategy to find the best set of material parameters that reproduce each of the 14 indentation tests (see more details in [3]). The result of the material parameters were later spatially averaged to obtain a single value characterizing the brain that was used over the entire domain of the finite element models. Table 1 summarize the averaged quantities over the 14 samples.

2.7. Finite element simulations

The initial condition is a uniform velocity $\mathrm{v}_0 = 0.1$m/s at time $\mathrm{t}_0 = 0$s in all the nodes of the model, making a straight trajectory with a predefined displacement. Then, a linear deceleration beginning at t> 0 up to $\mathrm{t}_1 = 25$ms is followed by an imposed zero velocity at the nodes that belong to the outer surface of the model, corresponding with the skull, until the final time of simulation $\mathrm{t}_f = 50$ms. An adaptive time increment scheme was used to speed-up the simulations. We use the finite element software Abaqus [60] to solve the dynamic simulation. The transient dynamic problem is solved explicitly in time ensuring stability criteria. The material models are implemented in user subroutines. The problem is parallelized and solved in a computer cluster with 5 nodes with 24 cores Intel Xeon E5-2650L v3 (1,8GHz, 12N/24S, 9.60GT/s i 65W) and 256 GB RAM memory.

3. Results

3.1. Mechanical response of mouse, macaque and human brains

We use the baseline elastic and viscoelastic parameters obtained by performing standard indentation tests on mouse brain slices, following the procedure described in Materials and Methods

to compute the mechanical response of the brain models. We used the geometric model of the brain of three different mammalian species: a model of human brain (GI ≈2.5), a rhesus macaque (GI≈1.75), and a common mouse (GI≈1) using 3D MRI images from which we extracted polygonal surfaces after filtering and segmentation (see Material and Methods for details). In our simulation, an impact load was applied laterally to the brains and results of the maximum principal strain, maximum principal stress, maximum shear stress and pressure were computed. These mechanical variables are widely used in brain damage mechanics [17, 71]. As expected, the mechanical response varied dramatically between species due to the large differences in brain mass (data not shown). For instance, the mass of the human brain is about 120 times larger than the mass of the mouse brain. Hence the same impact induces much higher inertial forces within the brain and no sensible comparison can be obtained.

3.2. Analysis of mass-scaled brain models

To take into account the variation in mass and isolate the role of the topological differences among species, we scaled the volumes of the mouse and macaque brains so that they have the same mass as the human brain and computed the mechanical response of these three mass-scaled brains. We create a probability distribution function (PDF) by fitting a kernel-smoothing distribution of the maximum accumulated value over time of the variables of interest in all nodes of the finite element mesh. We choose a kernel distribution in order to avoid making assumption about the distribution of the data. The estimation of the PDF is given by

$$\hat{f}_h(x) = \frac{1}{nh} \sum_{i=1}^{n} K\Big(\frac{x - x_i}{h}\Big), \tag{12}$$

where n is the sample size, K is the kernel function, h>0 is the bandwidth and x represent the sample data.

The PDF provides a measure of the relative volume of brain tissue, subjected to a specific value of the mechanical variables. Doing so we can analyze quantitatively the differences in the mechanical variables, compare the maximum values of the variables and the distribution of the variable values for the brain models. Fig. 2 shows the results of the PDF and the map of mechanical variables in the brain models.

The PDF along the three brain models, shown in Fig. 2(a-d), indicate that for every value of the mechanical variables the same relative amount of tissue subjected to that mechanical state would be obtained for the human and macaque models. However, we see that the mouse-scaled brain has a different response for all mechanical variables, suggesting that the GI of mammalian brains modify the amount of tissue that suffers the range of maximum mechanical stimuli under external loads.

Fig. 2(e-m) shows how these mechanical variables are distributed in space by only showing elements subjected to values higher than a given critical value. This figure demonstrate that the spatial distribution of the mechanical variables are significantly different along the three models. In the human brain the locations reaching a high value are highly dispersed throughout the brain. In the mouse model, the maximum principal stress and pressure are localized in the lateral part of the brain along the zone of impact and both the maximum principal strain and shear stress are localized in mid regions of both hemispheres. These results clearly suggest that topological differences modify not only the values of stresses and strains in the brain but also their spatial distribution. In addition, the fact that high values of stresses are disperse through the brain as the GI increases suggests that the folding pattern of the mammalian brain could act as a damping system to reduce mechanical damage for high-mass brain mammals.

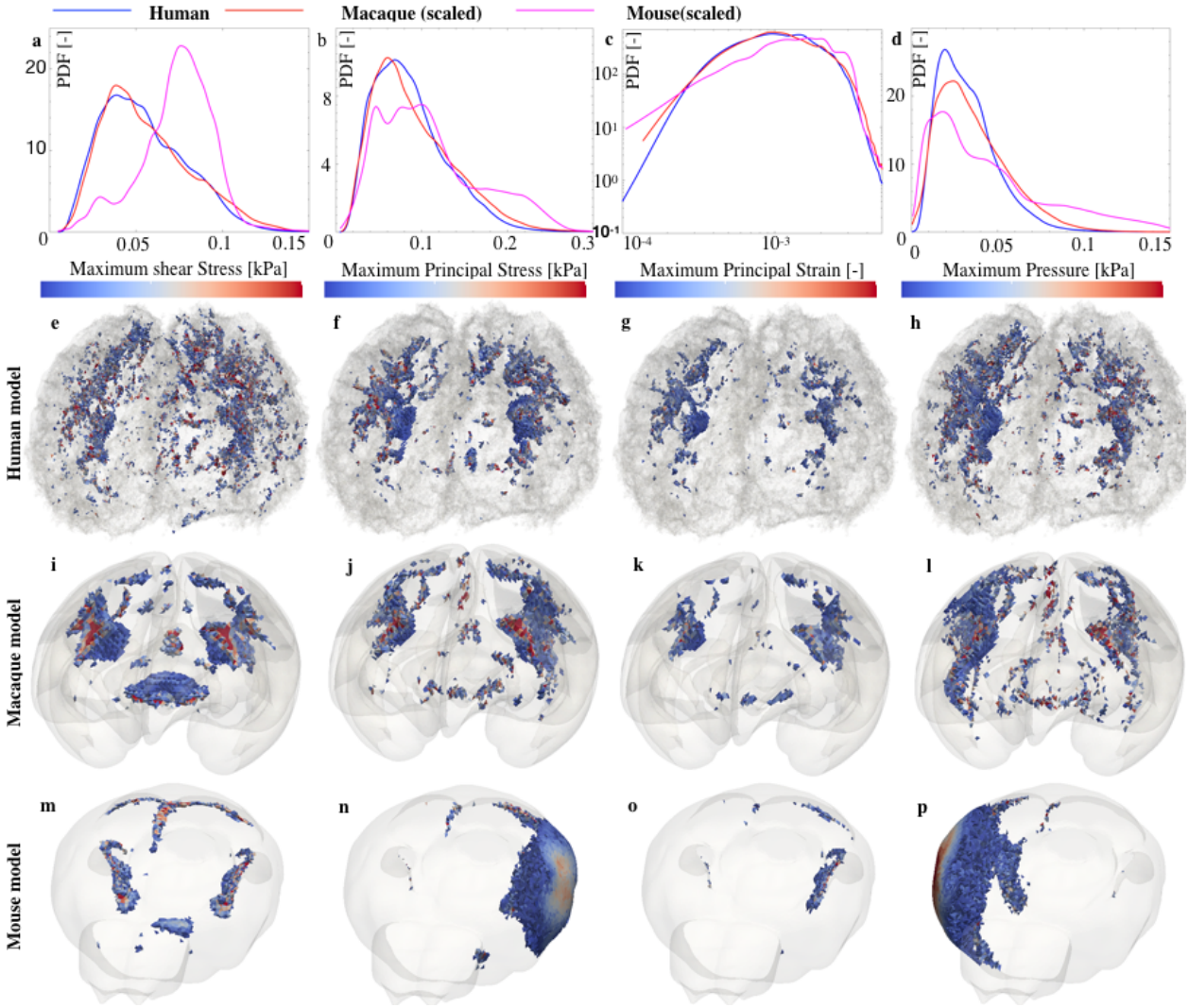

Figure 2: PDF distribution for the maximum shear stress (a), maximum principal stress (b), maximum principal strain (c) and maximum pressure (d) for the mouse (pink), macaque (red) and human (blue) models. The mechanical variables are plotted over the human (e-h), macaque (i-l) and mouse brain models (m-p). Only elements with a maximum shear stress (e,i,m), maximum principal stress (f,j,n), maximum principal strain (g,k,o) and pressure (h,l,p) with values higher than 0.12kPa, 22kPa, 4.10^{-3} and 0.1kPa, respectively, are shown. The human and macaque-scaled models behave similarly, with the curves for all mechanical variables overlapping very closely. For the maximum principal stress and pressure, we observed that the mouse model increases the PDF (i.e. the relative amount of tissue) subjected to the highest values, 0.2-0.3 kPa and 0.1-0.15 kPa, respectively. The maximum shear stress also presents a significant increase of the amount of tissue subjected to a shear stress of $\approx$ 0.1 kPa.

3.3. Analysis of elastic and viscous response of the brain

To investigate the relative effect of topological differences compared to the effect of material properties we vary the elastic and viscoelastic properties of the brain tissues in our simulations. We took the macaque model as control as an intermediate folding case between the human and the mouse model. First, we increased the Young's modulus to simulate a tissue that is either 2.5 times softer or 2.5 times stiffer. This range of stiffness covers previously reported values [51, 18, 12, 6, 40, 3]. Second, we modified the viscoelastic behavior of the brain. We took the results of our mechanical tests as control and compared the results with an elastic model, without viscoelastic behavior. Then, we considered a more viscous tissue by using the values reported in [6] with two Prony terms ($g_1 = 0.599$kPa, $g_2 = 0.241$kPa, $\tau_1 = 3.49$s, $\tau_2 = 298.55$s). The PDF for the four mechanical variables of interest are shown in Fig. 3.

Despite large variation of the tissue elastic properties, the simulations showed similar response for the maximum principal stress for the three values of the elastic properties. As expected, the distribution of principal strain and pressure of the softer material moved to the higher values of the variables. In addition, the amount of tissue subjected to the higher value of the variable visibly increased. The stiffer material moved the PDF of maximum shear stress to the right, i.e to higher values of the variables. However, we did not observed a non-uniform increase in the amount of tissue subjected to the higher values of the mechanical variables, as found in the mass-scaled models. Qualitatively, these changes are similar to the variations in the viscoelastic properties. Quantitatively, the variations in the amount of tissue for the maximum principal strain and pressure of the non-viscoelastic model clearly show a large increase of the amount of tissue subjected to large strain and pressure values. Note, however, that this is expected. In the absence of viscosity, there is no damping in the system and large stresses are expected. These results indicate that variations of the brain material response, such as elastic and viscoelastic properties, modify the state of stresses and strains in a uniform way. Our results also indicates that no changes for the amount of tissue subjected to specific ranges of the mechanical variables are observed for those realistic combinations of material parameters.

3.4. Topological differences dictate the mechanics of mammalian brains

To investigate the differences between mechanical properties and topological features in brain mechanics, we considered variations in the stiffness and viscoelastic parameters as well as the three mammal models. We were interested in investigating whether variations of mechanical properties are more or less relevant than differences in the folding pattern of the brain. We normalized the PDF of all models with respect to the macaque brain model, scaled to the human brain mass, with the mechanical values of our experiments which we took as the control case. Fig. 4 shows the normalization for the 4 variables of interests. We are interested in regions of higher values of the mechanical variables, identified as those lying on the right-hand side of the line marked as low-stress and low-strain regime in Fig. 4. We assume that variations in the lower regimens have no effect on possible damages. We are also interested in normalized values larger than one, meaning an increase in the value of the mechanical variable of interest.

The stiffer material and the mouse-scaled model show a higher increase of brain tissue subjected to the high shear stress. The mouse-scaled brain is the only model that shows an increase of amount of tissue under the highest values of maximum principal stress. The mouse-scaled model also shows a remarkable increase of strain for the larger strain values. However, this increase was higher for the softer material and even higher for the non viscoelastic model. The larger increase of tissue for higher values of pressure was found, taking aside the non viscoelastic model, for the mouse-scaled and the softer models. Therefore, our results indicate that for viscoelastic brains, the GI, i.e. the folding pattern in mammalian brains, is the most important feature that modifies brain mechanics

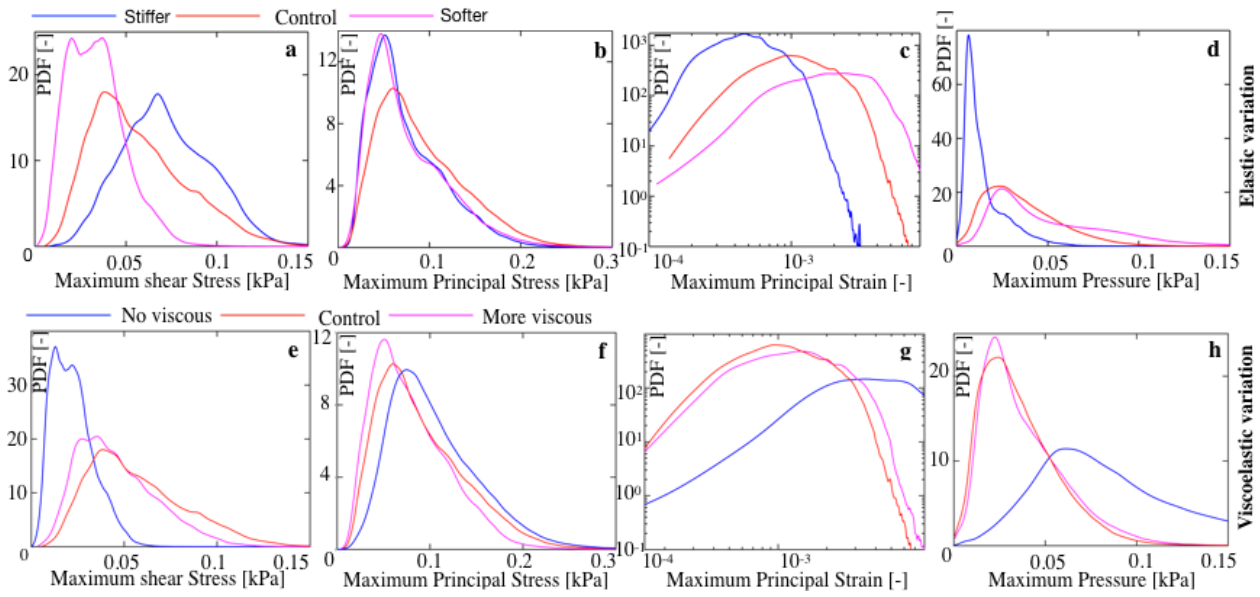

Figure 3: Variations of the elastic properties, for the control (red) a softer (blue) and a stiffer(pink) material: Maximum shear stress (a), maximum principal stress(b), maximum principal strain(c) and maximum pressure(d). Variations of the viscoelastic properties, for the control (red) a non-viscous model (blue) and a more viscous material (pink) : Maximum shear stress (e), maximum principal stress(f), maximum principal strain(g) and maximum pressure(h).

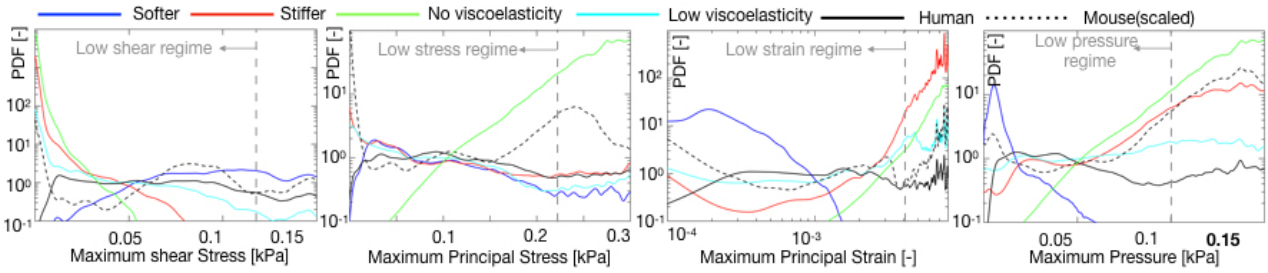

Figure 4: Normalized PDF with respect to the control model for the maximum shear stress (a), maximum principal stress (b), maximum principal strain (c) and pressure (d). Dashed lines represent the threshold level stablished to plot the finite element in Fig. 2, which represent a transition from low-level to a high-level mechanical values.

and for this reason it is a crucial quantity compared to elastic and viscoelastic variations in brain mechanics.

4. Discussion

The mechanical environment of mammalian brain plays a fundamental role in many brain disorders such as tumor growth [29, 8], inflammation [1] or in TBI [4, 5]. During the last decade, the research on brain mechanics has been focused on determining the mechanical properties, elastic and visco-elastic, of mammalian brains [51, 18, 12, 6]. Lately, the internal structure of the brain, made of a vast network of neuronal structures, is being also analyzed to determine the its mechanical role in brain mechanics. Mechanical and structural models have been included into computational

simulation to determine the overall mechanical response of the brain under static and dynamic loads.

Computational simulations have allowed to study brain mechanics in human models which is not available for controlled experimental settings for TBI, tumor growth or neurosurgical procedures, among others. However, important geometrical simplifications in the morphology of brain models have been used, which is central not only to analyze species-specific geometries but also to scale mechanical variables from more feasible animal tests to human research [34, 72]. For example, a large number of widely-used finite element brain models in literature describes human brain without the characteristic folding pattern [36]. Today new advances in MRI imaging and supercomputing resources have opened the door to high-fidelity and patient-specific brain models. The use of this new generation of accurate and precise computational models provide simulation platforms able to test scenarios often impossible by experimental and medical means. However, no study has analyzed how the mechanical response differ when the actual folding pattern of different species are considered or when highly accurate morphological brain models are used in comparison with featureless models.

Here, we used computational dynamic models to analyze what is the effect of the morphology in the mechanics of the brain. We found that the GI plays a fundamental role in the overall mechanical response of the brain. We also showed that topological diversity in brain models is more important than the differences in mechanical properties of the brain. Indeed, different folding patterns modified not only the stresses and strains in the brain but also its spatial distribution.

An important application of our results is TBI [22, 54, 72]. Literature on computational models for TBI is extensive (see [38, 17, 41, 71, 42] among many others). Here, we used an impact load to demonstrate our hypothesis but did not fully explore its implications for TBI as a more detailed model of impact would be needed. These studies would require a systematic validation of the models from published data [65, 28] and a larger set of impact conditions, including rotational accelerations, different velocity conditions, and blast loading [49, 34].

All results presented here were carried out with linear tetrahedral elements. It is known that linear tetrahedral elements underperform linear hexahedral elements. But the differences would be mostly limited to error in displacement and locking behavior, which did not occur in our simulations. Although it is also known that the performance of quadratic tetrahedral elements have an outstanding behavior, we should also consider the cost of creating structured meshes for high fidelity geometric models as the ones considered here. Some of our simulations were highly expensive even with the low demanding linear tetrahedral elements. However, given that our goal is the comparison between models, the same errors would appear in all models.

We also made some assumptions in the reconstructed geometries and in modeling. We simplified the definition of ventricles and the cerebellum. We did not model the CSF as a fluid or the vasculature, which would require complex and extremely demanding fluid-structure interaction simulation. Brain vasculature is very relevant for blood and nutrient supplies to the brain but only represents less than 3% of the total volume. The mechanical role of the vasculature could be included by using the mechanical properties obtained through mechanical test. However, for large vessels both meshing and proper boundary conditions would be computationally prohibitive. Finally, we also omitted tissue anisotropy that is believed to be relevant for the analysis of TBI and may be central for an accurate evaluation of TBI descriptors (see, for example, [41, 71, 9], among many others). However, recent works have shown that mechanical testing does not show any significant tissue anisotropy, and that the mechanical response of the brain tissue can be well described with or without considering explicitly the anisotropy [7, 47]. Similarly, it was also shown in the context of TBI that the time response of a FE model with and without explicit consideration of the anisotropic structure followed the same evolution in time and only minimal differences in the

maximum values were observed [23]. Hence, these works suggest that anisotropy would not change the conclusions of our study.

5. Conclusion

We showed that the brain shape, measured by the GI, plays a key role on the overall mechanical response of the brain. Highly folded brains behave mechanically differently than smoother brains and the use of smooth human brains in simulation may lead to biased results. We show that mechanical variables such as strain and stress are significantly different in magnitude along models with different GI. We showed that smooth brain patterns with GI≈1 increase the amount of tissue that experience high values of mechanical variables under external mechanical loads. We also demonstrated that these values where differently located along models with different folding patterns. We have shown that in brains with more folds, as in humans, the regions of high stresses and strains tend to be more diffused while in smoother brains, the same variables are localized in specific regions.

Therefore, topological features are important to the mechanics of mammalian brains and models must include realistic geometries to obtain relevant computational mechanics results. This is particularly important for any predictions related to brain damage. Given the ethical aspects on human experimentation, our findings underline the role of geometric measures such as the GI when comparing species. Whereas many scaling laws between different species have been proposed such as brain and body mass-related laws [56] or impedance and protective tissues scaling laws [34], we do not yet have scaling laws for brain models with different folding patterns. These laws will be fundamental for our understanding of brain and damage mechanics.

Acknowledgments P.S has been supported by the Generalitat de Catalunya under grants 2017-SGR-1278. N.A acknowledge funding from the European Research Council under the European Union's Seventh Framework Programme (FP/2007–2013)/ERC grant agreement no. [615170]. This work was supported by a Engineering and Physical Sciences Research Council grant to Alain Goriely (EP/R020205/1).

[1] O. Aktas, O. Ullrich, C. Infante-Duarte, R. Nitsch, and F. Zipp. Neuronal damage in brain inflammation. *Arch. Neurol.*, 64(2):185–189, feb 2007.

[2] S. Angeli, K. E. Emblem, P. Due-Tonnessen and T. Stylianopoulos Towards patient-specific modeling of brain tumor growth and formation of secondary nodes guided by DTI-MRI. *NeuroImage Clin.*, 20:664 - 673, 2018.

[3] N. Antonovaite, S. V. Beekmans, E. M. Hol, and W. J. Wadman. Regional variations in stiffness in live mouse brain tissue determined by depth-controlled indentation mapping. *Sci. Rep.*, 8(12517):1–11, 2018.

[4] P.V. Bayly, T.S. Cohen, E.P. Leister, D. Ajo, E.C. Leuthardt, and G.M. Genin. Deformation of the human brain induced by mild acceleration. *J Neurotrauma*, 22(8):845–856, aug 2005.

[5] R.R. Benson, S.A. Meda, S. Vasudevan, Z. Kou, K.A. Govindarajan, R.A. Hanks, S.R. Millis, M. Makki, Z. Latif, W. Coplin, J. Meythaler, and E.M. Haacke. Global White Matter Analysis of Diffusion Tensor Images Is Predictive of Injury Severity in Traumatic Brain Injury. *J. Neurotrauma*, 24(3):446–459, mar 2007.

[6] S. Budday, R. Nay, R. de Rooij, P. Steinmann, T. Wyrobek, T.C. Ovaert, and E. Kuhl. Mechanical properties of gray and white matter brain tissue by indentation. *J. Mech. Behav. Biomed. Mater.*, 2015.

[7] S. Budday, G. Sommer, C. Birkl, C. Langkammer, J. Haybaeck, J. Kohnert, M. Bauer, F. Paulsen, P. Steinmann, E. Kuhl and G.A.Holzapfel. Mechanical characterization of human brain tissue. *Acta Biomat.*, 48:319:340, 2017.

[8] D.T. Butcher, T. Alliston, and V.M. Weaver. A tense situation: forcing tumour progression. *Nat Rev Cancer*, 9(2):108–122, feb 2009.

[9] R.W. Carlsen and N.P. Daphalapurkar. The importance of structural anisotropy in computational models of traumatic brain injury. *Front. Neurol.*, 6:28, 2016.

[10] H.L. Cater, L.E. Sundstrom, and B. Morrison 3rd. Temporal development of hippocampal cell death is dependent on tissue strain but not strain rate. *J. Biomech.*, 39(15):2810–2818, 2006.

[11] S. Chatelin, A. Constantinesco, and R. Willinger. Fifty years of brain tissue mechanical testing : From in vitro to in vivo investigations. *Biorheology*, 47:255–276, 2010.

[12] S. Chatelin, C. Deck, and R. Willinger. An anisotropic viscous hyperelastic constitutive law for brain material finite-element modeling. *J. Biorheol.*, 27(1-2):26–37—-, 2013.

[13] A.O. Cifuentes, A. Kalbag. A performance study of tetrahedral and hexahedral elements in 3-D finite element structural analysis. *Fininte Elem. Anal. Des.*, 12: 3?4, 1992.

[14] R. Cloots, H. Gervaise, J. van Dommelen. Biomechanics of Traumatic Brain Injury: Influences of the Morphologic Heterogeneities of the Cerebral Cortex. *Ann Biomed Eng* 36: 1203, 2008.

[15] M. Colella, F. Camera, F. Capone, S. Setti, R. Cadossi, V. Di Lazzaro, F. Apollonio, M. Liberti. Patient Semi-specific Computational Modeling of Electromagnetic Stimulation Applied to Neuroprotective Treatments in Acute Ischemic Stroke. *Sci Rep.*, 10, 2945, 2020.

[16] D.J. Cooper, J.V. Rosenfeld, L. Murray, Y.M. Arabi, A.R. Davies, P. D'Urso, T. Kossmann, J. Ponsford, I. Seppelt, P. Reilly, and R. Wolfe. Decompressive Craniectomy in Diffuse Traumatic Brain Injury. *N Engl J Med*, 364(16):1493–1502, mar 2011.

[17] C. Deck and R. Willinger. Improved head injury criteria based on head FE model. *Int. J. Crashworthiness*, 13(6):667–678, 2008.

[18] J. A. W. van Dommelen, T. P. J. van der Sande, M. Hrapko, and G. W. M. Peters. Mechanical properties of brain tissue by indentation: Interregional variation. *J. Mech. Behav. Biomed. Mater.*, 3(2):158–166, feb 2010.

[19] T. L. Fletcher, B. Wirthl, A. G. Kolias, H. Adams, P.J.A. Hutchinson, M.P. F. Sutcliffe. Modelling of Brain Deformation After Decompressive Craniectomy. *Ann Biomed Eng.* , 44(12): 3495–3509.

[20] P.J. Flory. Thermodynamic relations for high elastic materials. *T. Faraday Soc.*, 57:829–838, 1961.

[21] T. Gerriets, E. Stolz, M. Walberer, C. Müller, A. Kluge, A. Bachmann, M. Fisher, M. Kaps, and G. Bachmann. Noninvasive Quantification of Brain Edema and the Space-Occupying Effect in Rat Stroke Models Using Magnetic Resonance Imaging. *Stroke*, 2004.

[22] J. Ghajar. Traumatic brain injury. *Lancet*, 356(9233):923–929, 2000.

[23] C. Giordano, R.J. Cloots, J.A. van Dommelen, S. Kleiven. The influence of anisotropy on brain injury prediction. *J. Biomech.*, 47(5):1052–9, 2014.

[24] A. Goriely, M.G.D. Geers, G.A. Holzapfel, J. Jayamohan, A. Jérusalem, S. Sivaloganathan, W. Squier, J.A.W. van Dommelen, S. Waters and E. Kuhl. Mechanics of the brain: perspectives, challenges, and opportunities. *Biomech Model Mechanobio*, 14:931, 2015.

[25] A. Goriely, S. Budday, E. Kuhl, Neuromechanics: from neurons to brain. *Adv. Appl. Mech.* 48 (2015) 79-139.

[26] A. Goriely, J. Weickenmeier, E. Kuhl (2016) Stress singularities in swelling soft solids. *Phys. Rev. Lett.* 117:138001

[27] A. Goriely, *The Mathematics and Mechanics of Biological Growth*, Springer Interdisciplinary and Applied Mathematics (2017).

[28] W. N. Hardy, M. J. Mason, C. D. Foster, C. S. Shah, J. M. Kopacz, K. H. Yang, and A. I. King A Study of the Response of the Human Cadaver Head to Impact. *Stapp Car Crash J.*, 51: 17–80, 2007.

[29] G. Helmlinger, Paolo A. Netti, Hera C. Lichtenbeld, Robert J. Melder, and Rakesh K. Jain. Solid stress inhibits the growth of multicellular tumor spheroids. *Nat. Biotechnol.*, 15:778–783, 1997.

[30] J. Ho and S. Kleiven Can sulci protect the brain from traumatic injury?" *J Biomech,* 42(13):2074–2080, 2009

[31] E. Hohlfeld and L. Mahadevan. Unfolding the sulcus. *Phys. Rev. Lett.*, 106(10):1–4, 2011.

[32] M. Holland, S. Budday, A. Goriely, and E. Kuhl. Symmetry breaking in wrinkling patterns: Gyri are universally thicker than sulci. *Phys. Rev. Lett.*, 121(22):228002, 2018.

[33] X. Huang, H. Chafi, K.L. Matthews, O. Carmichael, T. Li, Q. Miao, S. Wang, G. Jia. Magnetic resonance elastography of the brain: A study of feasibility and reproducibility using an ergonomic pillow-like passive driver. *Magn. Reson. Imaging*, 59:68–76, 2019.

[34] A. Jean, M.K. Nyein, J.Q. Zheng, D.F. Moore, J.D. Joannopoulos, and R. Radovitzky. An animal-to-human scaling law for blast-induced traumatic brain injury risk assessment. *Proc. Natl. Acad. Sci.*, 111(43):15310–15315, oct 2014.

[35] C.L. Johnson, E. H. Telzer. Magnetic resonance elastography for examining developmental changes in the mechanical properties of the brain. *Dev. Cog. Neurosci.*, 33:176–181, 2018.

[36] S.Ji, H. Ghadyani, R.P. Bolander, J.G. Beckwith, J.C. Ford, T.W. McAllister, L. Flashman, K.D. Paulsen, K. Ernstrom, S. Jain, R. Raman, L. Zhang, and R. M. Greenwald. Parametric comparisons of intracranial mechanical responses from three validated finite element models of the human head. *Ann Biomed Eng*, 42(1):11–24, jan 2014.

[37] T. Kaster, I. Sack, and A. Samani. Measurement of the hyperelastic properties of ex vivo brain tissue slices. *J. Biomech.*, 44(6):1158–1163, apr 2011.

[38] T.B. Khalil and W. Goldsmith and J.L. Sackman. Impact on a model head-helmet system. *Int. J. Mech. Sci.*, 16(9), 609 – 625, 1974.

[39] K.M. Kinnunen, R. Greenwood, J.H. Powell, R. Leech, Peter Charlie Hawkins, Valerie Bonnelle, Maneesh Chandrakant Patel, Serena Jane Counsell, and David James Sharp. White matter damage and cognitive impairment after traumatic brain injury. *Brain*,134(2):449?463, 2010.

[40] D. E- Koser, E. Moeendarbary, S. Kuerten, and K. Franze. Predicting local tissue mechanics using immunohistochemistry. *Biophys. J.*, 1088(9):2137-2147, 2015.

[41] R.H.Kraft, P.J. Mckee, A.M. Dagro, and S.T. Grafton. Combining the Finite Element Method with Structural Connectome-based Analysis for Modeling Neurotrauma: Connectome Neurotrauma Mechanics. *PLoS Comput Biol*, 8(8):e1002619—-, aug 2012.

[42] K. Laksari, M. Kurt, H. Babaee, S. Kleiven, and D. Camarillo. Mechanistic Insights into Human Brain Impact Dynamics through Modal Analysis. *Phys. Rev. Lett.*, 120(13):138101, 2018.

[43] G. E. Lang, P.S. Stewart, D. Vella, S.L. Waters, A. Goriely. Is the Donnan effect sufficient to explain swelling in brain tissue slices? *J. R. Soc. Interface* 11:20140123, 2014.

[44] A. Lopez-Rincon, C. Cantu, G. Etcheverry, R. Soto and S. Shimoda Function Based Brain Modeling and Simulation of an Ischemic Region in Post-Stroke Patients using the Bidomain. *J. Neuro. Meth.* 331:108464, 2020.

[45] C. L. Mac Donald, K. Dikranian, P. Bayly, D. Holtzman, and D. Brody. Diffusion Tensor Imaging Reliably Detects Experimental Traumatic Axonal Injury and Indicates Approximate Time of Injury. *J. Neurosci.*, 2007.

[46] P.R.Manger, M. Prowse, M. Haagensen, J. Hemingway. Quantitative analysis of neocortical gyrencephaly in African elephants (Loxodonta africana) and six species of cetaceans: comparison with other mammals. *J Comp Neurol*, 520(11):2430–2439, aug 2012.

[47] L.A. Mihai, S. Budday, G.A.Holzapfel, E. Kuhl and A. Goriely. A family of hyperelastic models for human brain tissue. *J. Mech. Phys. Solids*, 106:60–79, 2017.

[48] L. Marino. *The Anatomical Record: Advances in Integrative Anatomy and Evolutionary Biology,* 290:694–700, 2007.

[49] D.F. Moore, A. Jérusalem, M. Nyein, L. Noels, M.S. Jaffee, and R.A. Radovitzky. Computational biology ? Modeling of primary blast effects on the central nervous system. *Neuroimage*, 47, Supple(0):T10—-T20, aug 2009.

[50] M.C. Murphy, J.J. Huston, R. Clifford K.J. Glaser, M.L. Senjem, J. Chen, A. Manduca, J.P. Felmlee, R.L. Ehman, Measuring the characteristic topography of brain stiffness with magnetic resonance elastography. *PLoS One*, 12(8):1–14, 2013.

[51] F. Pervin and W. W. Chen. Dynamic mechanical response of bovine gray matter and white matter brain tissues under compression. *J. Biomech.*, 42(6):731–735, apr 2009.

[52] A. Post, A. Oeur, E. Walsh, B. Hoshizaki, and M.D. Gilchrist. A centric/non-centric impact protocol and finite element model methodology for the evaluation of American football helmets to evaluate risk of concussion. *Comput. Methods Biomech. Biomed. Engin.*, 2014.

[53] T.P. Prevost, G. Jin, M.A de Moya, H.B. Alam, S. Suresh, and Simona Socrate. Dynamic mechanical response of brain tissue in indentation in vivo, in situ and in vitro. *Acta Biomater.*, 7(12):4090–4101, dec 2011.

[54] M. Rusnak. Traumatic brain injury: Giving voice to a silent epidemic. *Nat. Rev. Neurol.*, 9(4):186–7, apr 2013.

[55] D. Sahoo, C. Deck, and R. Willinger. Finite element head model simulation and head injury prediction. *Comput. Methods Biomech. Biomed. Engin.*, 16(sup1):198–199, jul 2013.

[56] R.N. Saunders, X. G. Tan, S.M. Qidwai, and A. Bagchi. Towards Identification of Correspondence Rules to Relate Traumatic Brain Injury in Different Species. *Ann. Biomed. Eng.*, 2018.

[57] G. Sciumè, W.G. Gray, M. Ferrari, P. Decuzzi, B.A. Schrefler. Arch. Comput. Methods Eng.. *Ann. Biomed. Eng.*, 20(4):327–352, 2013.

[58] D.J. Sharp, G. Scott, and R. Leech. Network dysfunction after traumatic brain injury. *Nat. Rev. Neurol.*, 10(3):156–66, mar 2014.

[59] S. Su, T. White, M. Schmidt, C.Y. Kao, and G. Sapiro. Geometric computation of human gyrification indexes from magnetic resonance images. *Hum Brain Mapp*, 34(5):1230–1244, may 2013.

[60] Dassault Systèmes. Abaqus 2016. Analysis User's Manual.

[61] T. Tallinen, J.Y. Chung, F. Rousseau, N. Girard, Julien Lefèvre, and L. Mahadevan. On the growth and form of corticalconvolutions. *Nat. Phys.*, feb 2016.

[62] L. Tang, A.L. van de Ven, D. Guo, V. Andasari, V. Cristini, K.C. Li, X. Zhou. Computational Modeling of 3D Tumor Growth and Angiogenesis for Chemotherapy Evaluation. *PLoS One*, 9:1-12, 2014.

[63] P. Taylor and C.C. Ford. Simulation of Blast-Induced Early-Time Intracranial Wave Physics leading to Traumatic Brain Injury. *J. Biomech. Eng.*, 131(6):61007, apr 2009.

[64] M.T. Townsend, E. Alay, M. Skotak, and N. Chandra. Effect of Tissue Material Properties in Blast Loading: Coupled Experimentation and Finite Element Simulation. *Ann. Biomed. Eng.*, 2018.

[65] X. Trosseille, C. Tarrire, F. Lavaste. Development of a F.E.M. of the human head according to a specific test protocol. *36th Stapp Car Crash Conference*, SAE paper 922527, 1992.

[66] A. Trotta, J. M. Clark, A. McGoldrick, M.D. Gilchrist and A. NíAnnaidh Biofidelic finite element modelling of brain trauma: Importance of the scalp in simulating head impact. *Int. J. Mech. Sci.*, 16(9):609?25, 1974.

[67] W.J. Tyler. The mechanobiology of brain functio. *Nat. Rev. Neurosci.*, 13(12):867–878, 2012.

[68] M. Walberer, N. Ritschel, M. Nedelmann, K. Volk, C. Mueller, M. Tschernatsch, E. Stolz, F. Blaes, G. Bachmann, T. Gerriets. Aggravation of infarct formation by brain swelling in a large territorial stroke: a target for neuroprotection? *J. Neurosurg.*, 2008.

[69] J. Weickenmeier, M. Kurt, E. Ozkaya, M. Wintermark, K.B. Pauly, and E. Kuhl. Magnetic resonance elastography of the brain: A comparison between pigs and humans *J. Mech. Behav. Biomed. Mater.*, 77:702–710, 2018.

[70] J. Weickenmeier, P. Saez, C.A.M Butler, P.G. Young, A. Goriely, and E. Kuhl. Bulging brains. *J Elast.*,129(1-2): 197–212, 2017.

[71] R.M. Wright and K.T. Ramesh. An axonal strain injury criterion for traumatic brain injury. *Biomech. Model. Mechanobiol.*, 11(1-2):245–260—-, 2012.

[72] Ye Xiong, Asim Mahmood, and Michael Chopp. Animal models of traumatic brain injury. *Nat. Rev. Neurosci.*, 14(2):128–42, 2013.